SCIENCE CHINA
Chemistry

•ARTICLES•

July 2018 Vol.61 No.7: 797–805
https://doi.org/10.1007/s11426-017-8215-7

Removal of toxic metal ions using chitosan coated carbon nanotube composites for supercapacitors

Pin Hao[1†], Xiaoye Ma[1†], Junfeng Xie[1], Fengcai Lei[1], Liyi Li[2], Wenqian Zhu[1], Xin Cheng[1], Guanwei Cui[1] & Bo Tang[1*]

[1]*College of Chemistry, Chemical Engineering and Materials Science, Institute of Materials and Clean Energy, Collaborative Innovation Center of Functionalized Probes for Chemical Imaging in Universities of Shandong, Key Laboratory of Molecular and Nano Probes, Ministry of Education, Shandong Provincial Key Laboratory of Clean Production of Fine Chemicals, Shandong Normal University, Jinan 250014, China;*
[2]*Intel Corporation, Hillsboro OR 97124, USA*

Received November 30, 2017; accepted February 30, 2018; published online April 10, 2018

Environmental pollution and energy crisis are two major global challenges to human beings. Recovering energy from wastewater is considered to be one of the effective approaches to address these two issues synchronously. As the main pollutants in wastewater, toxic heavy metal ions are the potential candidates for energy storage devices with pseudocapacitive behaviors. In this study, toxic metal ions of Cr(VI) and Cu(II) are removed efficiently by chitosan coated oxygen-containing functional carbon nanotubes, and the corresponding equilibrium adsorption capacity is 142.1 and 123.7 mg g^{-1}. Followed by carbonization of metal ions-adsorbed adsorbents, Cu- and CrN-loaded carbon composites can be obtained. Electrochemical measurements show that the supercapacitor electrodes based on Cu- and CrN-loaded carbon composites have specific capacitance of 144.9 and 114.9 F g^{-1} at 2 mV s^{-1}, with superior electrochemical properties to pure chitosan coated carbon nanotubes after carbonization. This work demonstrates a new strategy for the resource-utilization of other heavy metal ions for energy devices, and also provides a new way to turn environmental pollutants into clean energy.

heavy metal ions adsorption, chitosan coated carbon nanotube, supercapacitor

Citation: Hao P, Ma X, Xie J, Lei F, Li L, Zhu W, Cheng X, Cui G, Tang B. Removal of toxic metal ions using chitosan coated carbon nanotube composites for supercapacitors. *Sci China Chem*, 2018, 61: 797–805, https://doi.org/10.1007/s11426-017-8215-7

1 Introduction

With the booming development of renewable energy devices to mitigate fossil energy depletion and environmental pollution, supercapacitors have attracted extensive researches because of high rate capability, high power density, excellent cycle stability and easy preparation [1–5]. These merits make them ideal candidates in various areas, such as supplementary power sources for electric vehicles, uninterruptible power supplies, memory back-up, and stand-by power systems [6–10]. A huge number of different materials have been prepared to build supercapacitors with excellent performance, such as carbon materials, metal-based materials, and conducting polymers [11–16]. Carbon materials, such as activated carbon, graphene, carbon nanotubes (CNTs) and carbon aerogels, possessing high electrical conductivity, excellent cycling stability, well-developed microstructure and established electrode production technologies, are widely used to obtain high-performance electrochemical double layer capacitors (EDLCs) [17–21]. However, due to the limited surface area, the specific capacitance of carbon materials is unsatisfactory [22]. Unlike carbon materials, metal-based materials such as RuO_2, MnO_2, NiO, Co_2O_3,

†These authors contributed equally to this work.
*Corresponding author (email: tangb@sdnu.edu.cn)

© Science China Press and Springer-Verlag GmbH Germany 2018

usually display higher specific capacitance because of Faradic redox reactions [23–27]. Nevertheless, the high cost of raw materials and the negative environmental impact of manufacturing process largely limit the widespread applications of most metal-based materials.

Heavy metal ions, such as Ni^{2+}, Cu^{2+}, Cr^{6+}, Pb^{2+}, are widely employed in many industrial applications, such as metal plating plants, smelting, and mining [28,29]. These heavy metal ions, once released into natural water, bring a significant threat to the environment and public health. The terrible consequence is that toxic heavy metal ions can be easily absorbed by living organisms in various ways and cause progressive poisoning effects on human health with gradual accumulation [30]. Although acute toxic incidents are rare, chronic toxicity can have a more serious impact in the long-term, leading to irreversible chronic illness of living organisms. Unlike some organic dyes, heavy metal ions are non-biodegradable and persistent environmental contaminants since they cannot be decomposed and metabolized [31]. Therefore, lots of effort has been devoted to removing toxic heavy metal ions. Removal of heavy metal ions from wastewater can be carried out by ion-exchange, chemical precipitation, neutralization, solvent extraction, coagulation and adsorption, etc [32–38]. Among these methods, adsorption is promising due to its easy operation, convenience and high efficiency. However, heavy metal ions removal process only eliminates the toxic metal ions from water. The adsorbents always lose their activity after several cycles of adsorption and need to be regenerated. The generation process is both time and energy consuming. In addition, during regeneration, the metal ions removed from the adsorbents can cause the secondary pollution. Therefore, reuse of the dead adsorbents after the heavy metal ions treatment is important. Recovering energy from the deactivated adsorbents is one of effective ways to resolve the above problems. As the main pollutants in waste water, many kinds of toxic metal ions such as Cu(II), Cr(VI), Ni(II), Co(II) and organic dyes with intrinsic redox functional groups such as methylene blue, indigoid dyes, are potential candidates for the pseudocapacitive materials [32]. There are some reports about adsorbents treated with organic dye pollutants from wastewater for supercapacitors [32,39]. Supercapacitors based on dye/adsorbents electrodes displayed excellent electrochemical performances. However, few works have been reported about converting toxic metal ions-loaded adsorbents into supercapacitors. Lu *et al.* [40,41] used commercial ion exchange resins to remove Cr(VI) and Mo(VI). Following carbonization of metal ions-containing adsorbents, they dissolved Cr or Mo from samples to prepare porous carbon for supercapacitors, resulting in the secondary pollution during dissolution. Direct utilization of the metal ions-loaded adsorbents to avoid the secondary contamination is the target that researchers are seeking to turn waste into values.

In this paper, to realize the transformation from toxic environmental pollutants to clean energy, toxic metal ions of Cr(VI) and Cu(II) are removed efficiently by chitosan-coated oxygen-containing functional carbon nanotubes. The corresponding equilibrium adsorption capacity is 142.1 and 123.7 mg g^{-1}. Followed by carbonization of metal ions-adsorbed adsorbents, Cu- and CrN-loaded carbon composites can be obtained. Electrochemical measurements show that the supercapacitor electrodes based on Cu- and CrN-loaded carbon composites demonstrate the specific capacitance of 144.9 and 114.9 F g^{-1} at 2 mV s^{-1}, displaying superior electrochemical properties to pure chitosan coated carbon nanotubes after carbonization. The metal-loaded adsorbents as new supercapacitor electrodes not only solve the waste disposal of regeneration process of deactivated adsorbents but also explore the new value of deactivated adsorbents as clean energy, both of which have great significance to environmental protection and sustainable development.

2 Materials and method

2.1 Oxygen-containing functionalization of pristine CNTs

Multiwalled CNTs with outer diameter of 10–15 nm were purchased from Chengdu Organic Chemicals Co., LTD. (China). The oxygen-containing functionalization of pristine CNTs was carried out following a reported process [42]: a total of 200 mg of pristine CNTs was added to 100 mL solution mixture with the concentrated H_2SO_4 and HNO_3 (volume ratio, 3:1). The mixture of pristine CNTs and acid was then maintained at 80 °C for 4 h without stirring. The functional CNTs were collected and washed with deionization (DI) water. The oxygen-containing functional CNTs were obtained by drying the sample at 60 °C overnight (labeled as F-CNTs).

2.2 Preparation of chitosan coated F-CNTs

100 mg Chitosan powder was dispersed into 100 mL 1 *v*% acetic acid solution, and 100 mg F-CNTs was added into the above blend with vigorous stirring. The mixture was under ultrasonic treatment for 10 min and then stirred for 1 h. 25 mL diluted ammonia solution (4 wt%) was added drop wise to the above solution. The mixture was heated at 60 °C and 10 mL oxalaldehyde (40 wt%) was added to the blend for the crosslinking of chitosan on the surface of F-CNTs. The as-prepared samples were collected and washed with diluted acetic acid and DI water several times, followed by vacuum-drying under 60 °C for 12 h, affording chitosan coated F-CNTs (labeled as CHIT/F-CNTs).

2.3 Equilibrium sorption experiments

The adsorption of toxic heavy metal ions on the as-prepared CHIT/F-CNTs using batch equilibrium technique was evaluated. Aqueous solutions of $K_2Cr_2O_7$ and $Cu(NO_3)_2$ with different concentrations (from 20 to 400 mg L^{-1}) were respectively used as Cr(VI) and Cu(II) simulated pollutant sources. The pH of Cr(VI) and Cu(II) aqueous solutions were adjusted to 3 and 6 by diluted HCl or NaOH solution, respectively. In general, an average of 10 mg CHIT/F-CNTs was added to 20 mL metal ions solution and shaken in a thermostatic water-bath shaker at 200 r min^{-1} for 11 h. When adsorption equilibrium was reached, the adsorbents and liquid were immediately separated by centrifugation at 10000 r min^{-1} for 8 min. The adsorbents were dried at 60 °C overnight for further carbonization to build supercapacitors. The concentrations of Cr(VI) and Cu(II) after adsorption were measured using Inductive Couple Plasma Mass Spectrometry (iCAP 7400, Thermo Fisher, USA). The amount of adsorbed metal ions per unit mass of adsorbent was evaluated by using the Eq. (1):

$$q_e = \frac{(C_0 - C_e)V}{M}, \quad (1)$$

where q_e is the adsorption capacity in mg g^{-1}; C_0 and C_e are the initial and equilibrium concentrations of metal ions solution in mg L^{-1}; V is the volume of the metal solution in L and M is the mass of the adsorbent in g.

2.4 Carbonization of metal ions-loaded adsorbents

The metal ions-loaded adsorbents were carbonized at 800 °C for 3 h in flowing N_2 at a rate of 3 °C min^{-1} in a tube furnace. The obtained metal-carbon hybrid samples were labelled as Cr-CHIT/F-CNTs and Cu-CHIT/F-CNTs. Scheme 1 is the graphical synthetic route.

2.5 Structural characterization

The morphology of adsorbents was characterized by a Hitachi SU8010 field-emission scanning electron microscope (FE-SEM, Janpan) and a Hitachi HT7700 transmission electron microscopy (TEM). X-ray photoelectron spectra (XPS) were recorded using a K-Alpha X-ray Photoelectron Spectrometer System (Thermo Fisher, USA). Fourier-transform infrared (FTIR) spectra were measured on ALPHA spectrometer (Bruker, Germany). Electron probe micro-analyzer (EPMA) was employed to confirm the adsorption of metal ions on adsorbents (EPMA-1720H, Shimadzu, Japan). X-ray diffractometer (D8 AVANCE, Bruker) over a 2 h scan range of 10°–80° was used to obtain the X-ray powder diffraction (XRD) patterns of the samples after carbonization. Element analyzer (PerkinElmer Instruments, Series II 2400, UK) was used to obtain the nitrogen content of the samples.

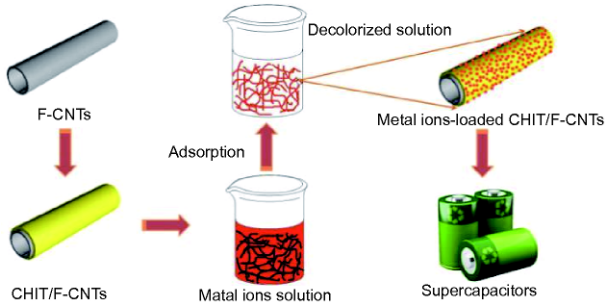

Scheme 1 Schematic illustration of the formation process of metal-carbon nanotube hybrid structures (color online).

2.6 Electrochemical measurements

Three-electrode devices were used to evaluate the electrochemical properties of the samples after carbonization. The working electrode was made of the active material and polyvinylidenefuoride (PVDF) with the weight ratio of 9:1. The slurry of the working electrode was made by mixing the activated sample and PVDF which was dissolved in *N*-methyl pyrrolidone (NMP) in advance (0.01 g mL^{-1}). After stirring for 12 h, the mixture was coated onto a stainless steel sheet with the size of 1 cm×1 cm. Then the prepared electrodes were dried at 60 °C overnight to remove NMP. A Ag/AgCl (saturated with KCl (aq.)) electrode and a platinum wire were used as the reference electrode and the counter electrode, respectively.

Asymmetric configurations were built in stainless cells with carbon fiber paper as the current collector and glassy fibrous paper as the separator. The sample of Cr-CHIT/F-CNTs or Cu-CHIT/F-CNTs acts as the positive electrode, and CHIT/F-CNTs after carbonization acts as the negative electrode. After the drying of the above-described slurry in three-electrode setup at 60 °C for 15 min, the mixture was rolled into a thin film. Followed by drying at 60 °C for 24 h to remove the NMP, the film was cut into circular slices with a diameter of 6 mm. According to the charge balance, the mass ratio of positive electrode (Cr-CHIT/F-CNTs or Cu-CHIT/F-CNTs) to negative electrode (CHIT/F-CNTs after carbonization) should be decided before assembling the asymmetric supercapacitor:

$$q_+ = q_-, \quad (2)$$

$$q = m \times C \times \Delta V, \quad (3)$$

$$\frac{m_+}{m_-} = \frac{C_- \times \Delta V_-}{C_+ \times \Delta V_+}, \quad (4)$$

where q is the charge, C is the specific capacitance obtained by the three-electrode setup, m is the mass of the electrode and ΔV is the potential window in the three-electrodes test.

0.5 mol L^{-1} H_2SO_4 solution was used as the electrolyte.

Cyclic voltammetric (CV), galvanostatic charging/discharging measurements (GCD) and electrochemical impedance spectroscopy (EIS) were performed using a CHI 660D Electrochemical Workstation (CH Instruments, China). The specific capacitance was calculated from CV curves collected from three-electrode test via $C = \int I\,\mathrm{d}t / mV$, where I is the current, V is the working potential window, and m is the mass of the active material on working electrode. The specific capacitance from galvanostatic charging/discharging curves was calculated according to the equation $C = It / mV$, where I is the discharge current, t is the discharge time, V is the working voltage window, and m is the weight of the active material on working electrode. The specific capacitance in the asymmetric two-electrode devices was calculated according to the CV curves based on the following equation $C = \int I\,\mathrm{d}t / MV$, where M is the total mass of the active materials on both electrodes.

3 Results and discussion

Morphologies of F-CNTs and CHIT/F-CNTs were characterized by FE-SEM. Figure 1(a) depicts the SEM image of F-CNTs without coating, indicating a good dispersion after oxygen-containing functionalization. From the enlarged image of F-CNTs, we can see F-CNTs with outer diameter of 10–15 nm display a snake-like shape with a smooth surface (Figure 1(b)). Figure 1(c, d) are the morphology of CHIT/F-CNTs. Snake-like one-dimensional nanostructures can be clearly seen, similar to nanotubes without coating. The surface of CHIT/F-CNTs is relatively uniform, being 20–30 nm in diameter, up to several tens of micrometers in length. Note that the diameter is slightly greater than those of F-CNTs due to the surface decoration, indicating the formation of chitosan coating on the surface of F-CNTs. Careful observation reveals that there is a little agglomeration after the surface coating because of the high viscidity of chitosan polymer.

TEM observation was employed to further investigate the microstructures of F-CNTs and CHIT/F-CNTs. Figure 2(a–c) are the TEM images of F-CNTs with different magnifications. The TEM image shown in Figure 2(a) further confirms that F-CNTs are mono-dispersed with the uniform diameter of 10–15 nm, consistent with the SEM results. From Figure 2 (b, c), we can see the inner diameter of F-CNTs is about 10 nm with the wall thickness about 2–3 nm. Figure 2(d–f) display the detailed structures of CHIT/F-CNTs. As shown in Figure 2(d), the nanotubes have a strong tendency to form bundles due to the viscous chitosan on the surface. The enlarged images of Figure 2(e, f) show that the blends exhibit a greater diameter in the range of 20–30 nm with the increase of the wall thickness to 5–10 nm, confirming the decoration

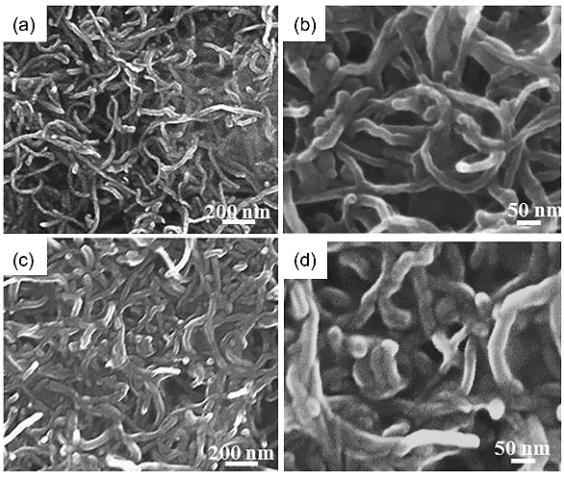

Figure 1 SEM images of F-CNTs (a, b) and CHIT/F-CNTs (c, d).

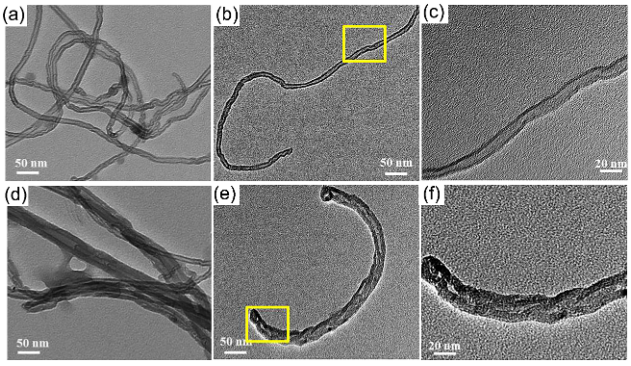

Figure 2 TEM images of (a–c) F-CNTs and (d–f) CHIT/F-CNTs (color online).

of chitosan on CHIT/F-CNTs.

XPS and FTIR spectra are given in Figure 3 to investigate the chemical composition and surface content of CHIT/F-CNTs. From the XPS results (Figure 3(a)), it can be observed that two dominant peaks appear at 284.5 and 531.5 eV in the XPS survey spectra of F-CNTS and CHIT/F-CNTs, corresponding to C 1s and O 1s. Furthermore, a characteristic peak of N 1s (400.1 eV) can be found in the sample of CHIT/F-CNTs, giving strong evidence for the existence of chitosan in CHIT/F-CNTs. The XPS analysis results are summarized and shown in Table S1 (Supporting Information online). The FTIR spectra are plotted in Figure 3(b), which demonstrate a clear distinction between F-CNTs, chitosan and CHIT/F-CNTs. The inset in Figure 3(b) is the enlarged spectrum of F-CNTs, which displays the O–H (2500–3500 cm^{-1}), C=O (1720 cm^{-1}) and C–O (1100 cm^{-1}) functional groups in F-CNTs, indicating the oxygen-containing functionalization of pristine CNTs [43]. For chitosan powders, the distinct peaks at 1590 and 1654 cm^{-1} correspond to the amide I band and amide II band. The peaks between 1000 and 1200 cm^{-1} are previously attributed to distinct vibrational modes of C–O–C, C–OH, and C–C ring vibrations. N–H stretching

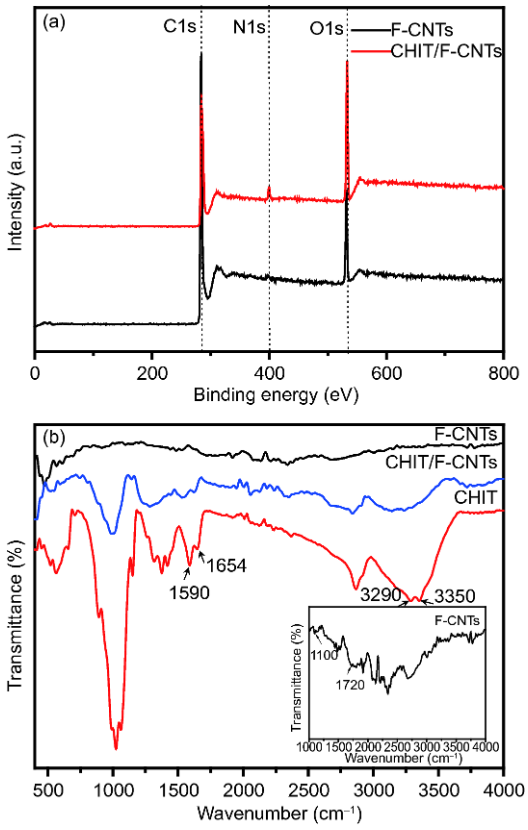

Figure 3 XPS (a) and FTIR (b) spectra of the samples (color online).

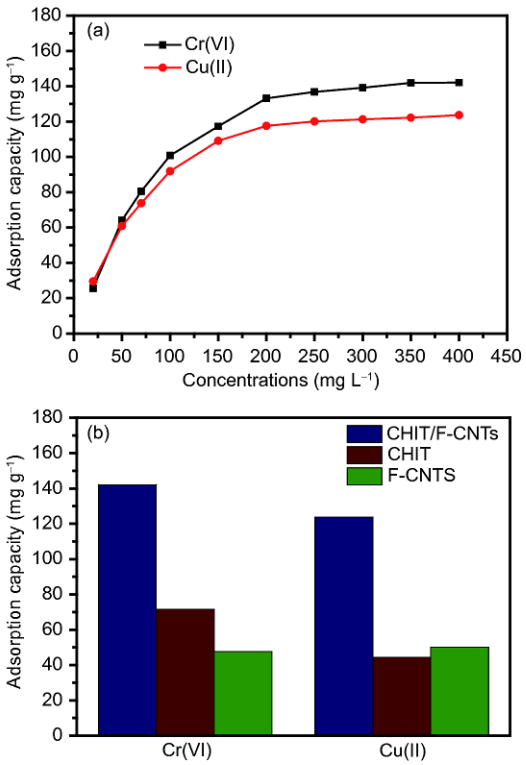

Figure 4 (a) Adsorption isotherms of Cr(VI) and Cu(II) with concentrations from 20 to 400 mg L^{-1} by CHIT/F-CNTs; (b) equilibrium adsorption capacity of different samples in metal aqueous solutions (color online).

and O–H stretching vibrations can be characterized by the broad peaks in the range of 3000–3600 cm^{-1} [44]. Similar results have been obtained in the case of FTIR spectrum of CHIT/F-CNTs, confirming the formation of chitosan in the blend. In order to calculate the loading weight of chitosan on carbon nanotubes, element analyzer was employed to obtain the content of nitrogen which is from the amino groups of chitosan in the samples. The nitrogen content of pure chitosan and CHIT/F-CNTs was 7.61% and 2.44%, respectively. Thus, it can be calculated that the loading weight of chitosan on the surface of F-CNTs is 0.47 mg mg^{-1} F-CNTs.

To evaluate the abilities of CHIT/F-CNTs for removal of heavy metal ions from aqueous solutions, adsorption isotherms of Cr(VI) and Cu(II) on CHIT/F-CNTs are plotted in Figure 4(a). From Figure 4(a), we can see the adsorption capacity of metal ions on adsorbents increases with increasing the initial metal ions' concentration. As shown in this plot, CHIT/F-CNTs display more affinity to Cr(VI) than Cu(II). The corresponding equilibrium adsorption capacity is 142.1 and 123.7 mg g^{-1}, respectively. This is because $Cr_2O_7^{2-}$ can be easily adsorbed on the protonated amino groups of chitosan in acidic condition. The efficient adsorption capacity of Cr(VI) and Cu(II) on CHIT/F-CNTs is much higher than many adsorbents, such as untreated plant waste, carbon adsorbents and inorganic adsorbents (Table S2). For comparison, the equilibrium adsorption capacities of chitosan and F-CNTs are also displayed in Figure 4(b). The results depict that CHIT/F-CNTs show the highest adsorption capacity than those two materials. This is because that amino, hydroxyl and carboxyl groups in the blends can provide huge number of adsorption sites for metal ions [45]. Moreover, chitosan coating on F-CNTs can prevent the agglomeration of dispersive F-CNTs, avoiding the decrease of adsorption sites caused by agglomeration. EMPA measurements were employed to confirm the adsorption of toxic metal ions on CHIT/F-CNTs (Figure S1, Supporting Information online). The spectra of CHIT/F-CNTs after adsorption display obvious peaks of Cr and Cu ions. The Langmuir and Freundlich adsorption models were used to analyse Cu(II) and Cr(VI) ions adsorption process [30].

$$C_e/q_e = C_e/q_m + 1/q_m K_L, \quad (5)$$

$$\ln q_e = (1/n)\ln C_e + \ln K_F, \quad (6)$$

where q_e is the equilibrium adsorption capacity (mg g^{-1}), C_e is the equilibrium concentration of metal ions in aqueous solution (mg L^{-1}), q_m is the maximum adsorption capacity (mg g^{-1}), K_L is the Langmuir equilibrium constant (L mg^{-1}), K_F (L g^{-1}) and n are the constants of Freundlich adsorption.

The parameters and related correlation coefficients (R^2) of the two adsorption models are summerized in Table 1. Apparently, the experimental data of Cu(II) and Cr(VI) ions on this absorbent fits better to the Langmuir adsorption model

Table 1 Adsorption isotherm parameters of Freundlich and Langmuir models for Cr(VI) and Cu(II) ions on CHIT/F-CNTs

Isotherm Parameters	Langmuir			Freundlich		
	q_m (mg g^{-1})	K_L (L mg^{-1})	R^2	n	K_F (L g^{-1})	R^2
Cr(VI)	146.5	0.03	0.998	2.42	15.61	0.857
Cu(II)	127.8	0.04	0.999	2.88	19.25	0.903

(R^2>0.99) than to the Freundlich isotherm, indicating that Cr(VI) and Cu(II) ions adsorb as a monolayer coverage on the surface of CHIT/F-CNTs. Based on the data of the Langmuir model, the maximum adsorption capacity of Cr (VI) and Cu(II) on CHIT/F-CNTs is calculated to be 146.5 and 127.8 mg g^{-1}, corresponding well to the results shown in Figure 4(a).

Carbonization of metal ions-loaded CHIT/F-CNTs after adsorption is necessary to obtain metal-carbon hybrid materials for supercapacitor electrodes. On one side, metal ions can be transformed to metallic materials to contribute pseudocapacitance through Faradic redox reactions. On the other side, the chitosan coating needs to be carbonized to enhance the electrical conductivity and double layer capacitance. The XRD patterns of Cr-CHIT/F-CNTs, Cu-CHIT/F-CNTs and CHIT/F-CNTs after carbonization are shown in Figure 5. Two broad peaks at 26.6° and 43.5° display in the XRD pattern of CHIT/F-CNTs after carbonization, corresponding to graphite basal plane (JCPDS card No. 26-1079). After carbonization, metal ions-loaded CHIT/F-CNTs were transformed to obtain metal-carbon hybrid materials. For the sample of Cu-CHIT/F-CNTs, the diffraction peaks at 43.3°, 50.4° and 74.1° match the respective (111), (200) and (220) planes of Cu (JCPDS card No. 04-0836), indicating phase transformation from Cu^{2+} to Cu due to the strong reduction by carbon. As for Cr-CHIT/F-CNTs, the detected peaks at 37.5°, 43.7°, 63.5°, and 76.2° can be assigned to the (111), (200), (220), and (311) planes of CrN (JCPDS card No. 11-0065), confirming the formation of CrN in Cr-CHIT/F-CNTs after carbonization. This is because $Cr_2O_7^{2-}$ can react with $-NH_2$ of chitosan at high temperature to form the phase of CrN due to the high activity of Cr. Figure S2 is SEM images of the samples after carbonization. As shown in Figure S2(a, b), Cu and CrN nanoparticles are distributed between carbon nanotubes. There are some agglomeration between the particles because of the sintering phenomenon. It further proved that the metal-carbon hybrid materials were successfully prepared through direct adsorption of toxic metal ions which were transformed to Cu or CrN after calcined at 800 °C for 3 h.

As a proof-of-concept, electrochemical performance of the metal-carbon hybrid materials after adsorption and carbonization was evaluated. Cyclic voltammetry (CV) tests were carried out using a three-electrode setup in an aqueous electrolyte of 0.5 mol L^{-1} H_2SO_4, and the results are demonstrated in Figure 6. For comparing and analyzing the electrochemical properties of metal-carbon hybrid materials, the CV curves of pure CHIT/F-CNTs after carbonization are also depicted. The CV curves of CHIT/F-CNTs after carbonization in the potential window of −0.2 to 0.5 V (vs. Ag/AgCl) display an quasi-rectangular and symmetric shape at various scan rates from 2 to 100 mV s^{-1}, implying near-ideal reversible standard double-layer capacitive behavior (Figure 6(a)). Different from the above results, metal-carbon hybrid materials, either Cr-CHIT/F-CNTs or Cu-CHIT/F-CNTs, exhibit the pseudocapacitive current responses, indicating that the Faradic redox reactions occurred on the surface of electrodes. Figure 6(b) shows the representative CV behavior of Cr-CHIT/F-CNTs in the potential range of 0–0.8 V (vs. Ag/AgCl) at various sweep rates. One couple of redox peaks can be observed in the approximately rectangular CV curves, indicating the co-existence of pseudocapacitive and double-layer capacitive characteristics in the sample. Electrochemical reactions can be expressed by the following equation:

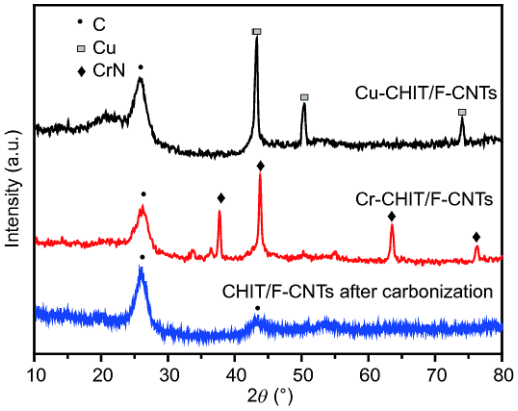

Figure 5 XRD patterns of Cr-CHIT/F-CNTs, Cu-CHIT/F-CNTs and CHIT/F-CNTs after carbonization (color online).

$$C+CrN+H^+ \leftrightarrow C\| H^+ + CrN \| H^+ + CrN\text{-}H^+, \quad (7)$$

where CrN||H^+ and C||H^+ stand for double-layer capacitive behavior and CrN–H^+ represents the pseudocapacitive behavior which is attribute to the intercalation/chemisorption of protons into the solid phase [46]. The plots in Figure 6(c) depict the CV curves of Cu-CHIT/F-CNTs in the voltage of −0.3 to 0.5 V (vs. Ag/AgCl). The shape of CV curves reveals discrepancy in a rectangle and the redox peaks are more

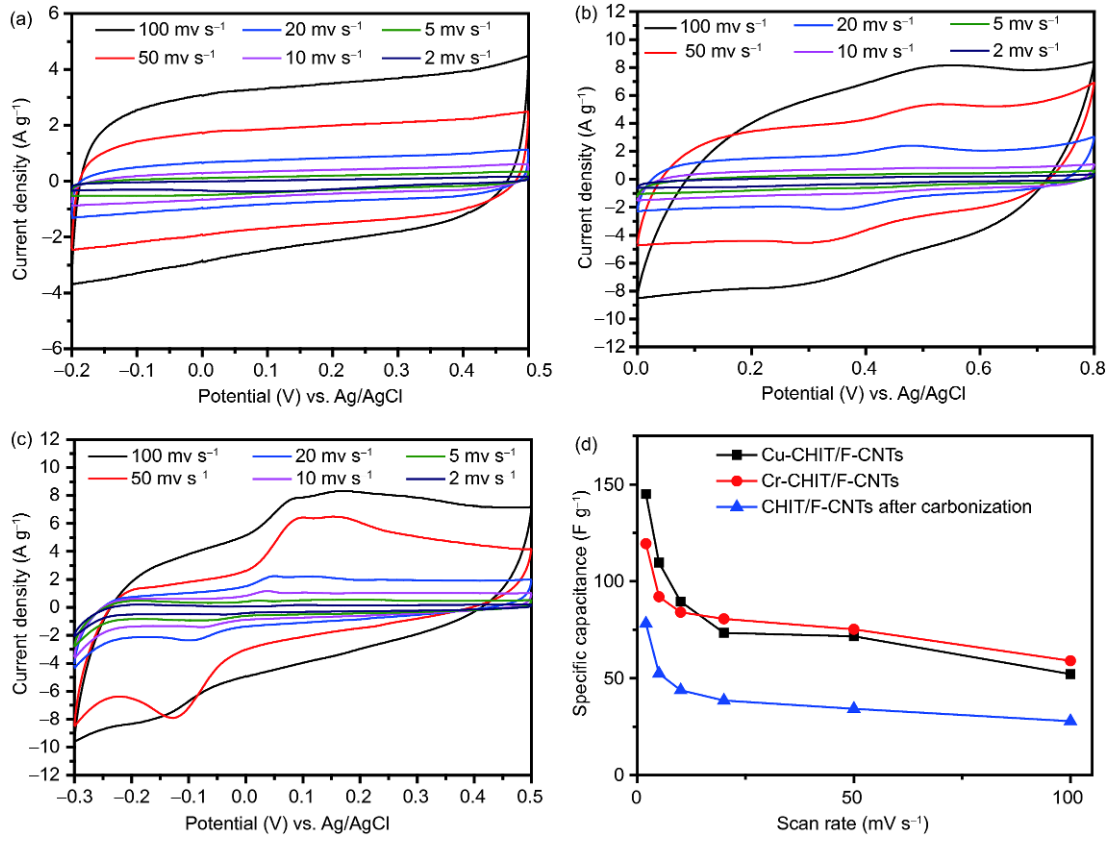

Figure 6 CV curves of CHIT/F-CNTs after carbonization (a), Cr-CHIT/F-CNTs (b), and Cu-CHIT/F-CNTs (c) at various scan rates in 0.5 mol L^{-1} H_2SO_4 aqueous electrolyte; (d) specific capacitance as a function of scan rate (color online).

obvious, indicating that the capacitive behavior of Cu-CHIT/F-CNTs is distinct from those of carbon-based electrode. The capacitive behavior of Cu-CHIT/F-CNTs can be explained by the following two parts: (1) the adsorption of abundant protons on the surface active sites forms C||H^+ for electrochemical double-layer capacitance and (2) Cu species contribute to the pseudocapacitance because of the Faradic redox reactions of Cu/Cu^+/Cu^{2+} [47,48]. Apparently, all curves remain a similar shape, and the current density increases with increasing sweep rate from 2 to 100 mV s^{-1}. It is noted that the current densities of Cr-CHIT/F-CNTs and Cu-CHIT/F-CNTs are higher than CHIT/F-CNTs after carbonization at the same scan rate, confirming the enhanced capacitance of metal-carbon hybrid materials. In order to exclude the influence of the stainless steel sheet, the comparison of CV curves between the stainless steel sheet and metal-carbon hybrid materials at the scan rate of 50 mV s^{-1} is also displayed in Figure S3. The capacitance of the stainless steel sheet is negligible. Figure 6(d) summarizes the specific capacitance of these samples from the CV curves as a function of sweep rate and the values are shown in Table S3. We can see that the electrochemical property of CHIT/F-CNTs after carbonization is inferior. Even at the scan rate of 2 mV s^{-1}, the specific capacitance is only 78.2 F g^{-1}. After the combination between Cu or CrN and CHIT/F-CNTs, the specific capacitance of metal-carbon hybrid materials is enhanced obviously. The specific capacitance of Cu-CHIT/F-CNTs is about 144.9 F g^{-1} at the scan rate of 2 mV s^{-1}, while Cr-CHIT/F-CNTs has the specific capacitance of 119.4 F g^{-1}, further implying the improvement of electrochemical properties due to the exist of Cu or CrN species. Though the sample of Cu-CHIT/F-CNTs displays the highest specific capacitance at 2 mV s^{-1}, the value at 100 mV s^{-1} is lower than Cr-CHIT/F-CNTs, indicating the poor rate capability. This may be caused by the following reasons. For one hand, the metallic copper on the surface of CHIT/F-CNTs after carbonization can impede the ion accessibility of carbon materials by effectively reducing the specific surface area during the electrochemical test. On the other hand, a slower Faradic redox reaction between copper and electrolyte ions leads to the unsatisfied rate capability [47]. The performance of the samples is similar with other electrodes which used for supercapacitors after toxic metal ions adsorption (100–200 F g^{-1}) [45,49]. Because the morphology and the loading weight of Cu and CrN did not be regulated, the specific capacitance of Cu-CHIT/F-CNTs and Cr-CHIT/F-CNTs is not outstanding compared with some professional electrodes prepared from the carbonization of mixtures of organic reagents or metal compounds. However, it is highly promising if one considers to recover energy from waste-

water. Electrochemical impedance spectroscopy (EIS) was also measured from 0.01 Hz to 100 kHz to demonstrate the electrochemical properties of the samples, and the results are depicted in Figure S4. The obtained Nyquist plots for all the samples consist of a linear line in the low frequency range followed by a semicircle in the high frequency region, standing for the diffusion resistance and charge transfer resistance (R_{ct}), respectively. The intercept of the spectrum with the horizontal axis represents the series resistance (R_s). The sample of Cu-CHIT/F-CNTs displays the smallest R_s (1.24 Ω) due to the introduction of metallic copper, implying the excellent conductivity of the sample. However, Cr-CHIT/F-CNTs display inferior electrical conductivity due to the exist of CrN in the sample (2.57 Ω). The R_{ct} values of Cu-CHIT/F-CNTs, Cr-CHIT/F-CNTs and CHIT/F-CNTs after carbonization are 6.68, 23.43 and 19.06 Ω, respectively.

Figure 7 depicts the charge-discharge behaviors of the samples in different voltage ranges at different current densities from 1 to 10 A g^{-1}. The galvanostatic charge-discharge curves of CHIT/F-CNTs after carbonization and Cr-CHIT/F-CNTs at various current densities show good symmetry and nearly linear slopes (Figure 7(a, b)). Consistent with the CV results, the plateaus and nonlinearity in the galvanostatic charge-discharge curves of Cu-CHIT/F-CNTs indicate the presence of Faradaic redox reactions, confirming that both the electrochemical double-layer adsorption and the Faradic redox reaction contribute to the energy storage in Cu-CHIT/F-CNTs (Figure 7(c)). Figure 7(d) is the specific capacitance calculated from the galvanostatic charge/discharge curves. The Cu-CHIT/F-CNTs electrode exhibits the highest specific capacitance of 83.5 F g^{-1} at the current density of 1 A g^{-1}, agreeing with the CV test results. Asymmetric two-electrode devices were assembled to further identify the electrochemical properties of Cr-CHIT/F-CNTs and Cu-CHIT/F-CNTs for practical applications (Figure S5). Unlike the three-electrode setup, from Figure S5, we can see when the sample of Cr-CHIT/F-CNTs or Cu-CHIT/F-CNTs acts as the positive electrode, and CHIT/F-CNTs after carbonization acts as the negative electrode, the current for electrical double layer capacitance overlaps with the current of redox reaction, leading to the disappearance of Faraday peaks in the CV curves of asymmetric two-electrode devices. Table S4 summarizes the specific capacitance of asymmetric devices from the CV curves as a function of sweep rate.

4 Conclusions

In summary, we have prepared new supercapacitor electrodes based on the metal-loaded chitosan coated oxygen-containing functional carbon nanotubes through a facile heavy metal ions adsorption and carbonization procedure. Cr(VI)

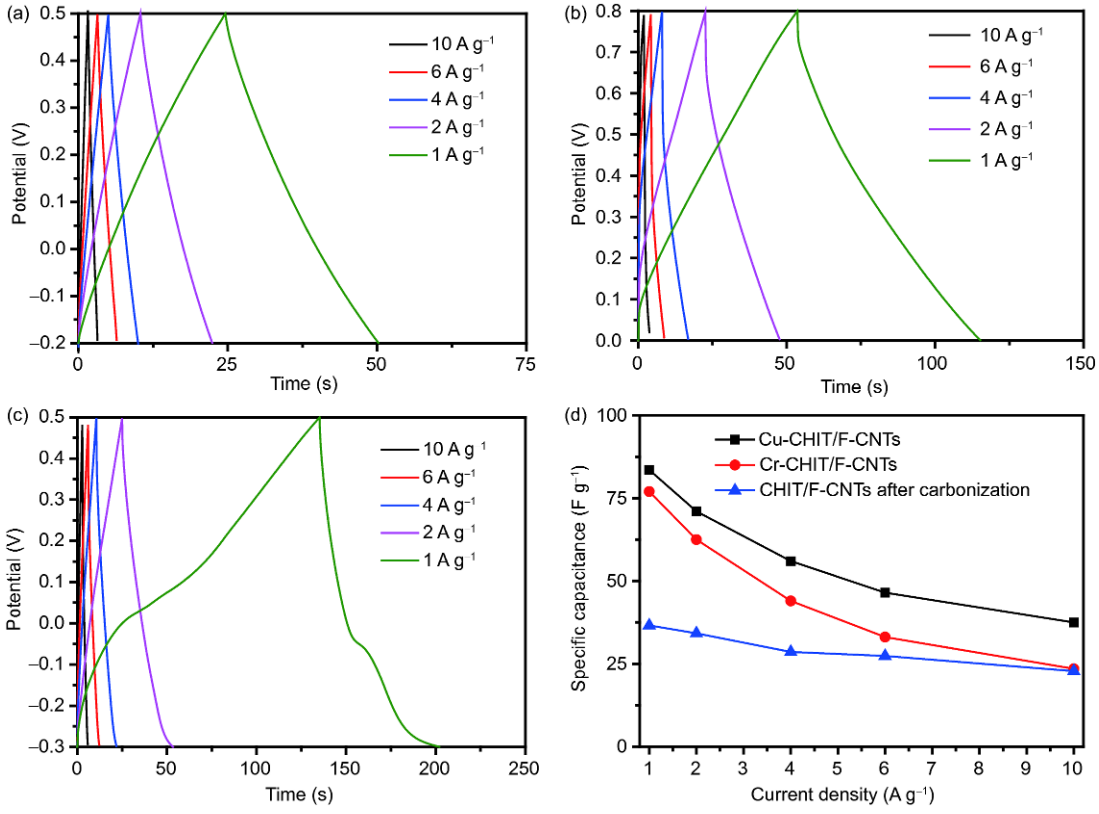

Figure 7 Charge-discharge curves of CHIT/F-CNTs after carbonization (a), Cr-CHIT/F-CNTs (b), and Cu-CHIT/F-CNTs (c); (d) specific capacitance as a function of current density (color online).

and Cu(II) can be removed efficiently from their aqueous solutions. Both the Cu- and CrN-loaded carbon materials exhibit superior capacitive behavior with specific capacitance of 144.9 and 119.4 F g^{-1} at 2 mV s^{-1}, almost two times higher than that of pure chitosan coated carbon nanotubes after carbonization. Although the electrochemical performance of some cases prepared from the carbonization of mixtures of organic reagents or metal oxides is superior to this work, the requirement of highly toxic reagents in these other cases can discourage their use in electrode preparation. The results of adsorption and electrochemical tests in this study have potential applications in waste water recovery and re-utilization of metal ions for energy storage. Thus, the presented work is highly promising because it demonstrates a novel route to turn toxic metal ions into energy, achieving energy storage and environment remediation simultaneously. The design also opens the door to utilize other environmental contaminants for clean energy.

Acknowledgements This work was supported by the National Natural Science Foundation of China (51602182, 21535004, 21390411) and Shandong Provincial Natural Science Foundation (ZR2016EMQ02, ZR2016BP07).

Conflict of interest The authors declare that they have no conflict of interest.

Supporting information The supporting information is available online at chem.scichina.com and link.springer.com/journal/11426. The supporting materials are published as submitted, without typesetting or editing. The responsibility for scientific accuracy and content remains entirely with the authors.

1 Sun H, Mei L, Liang J, Zhao Z, Lee C, Fei H, Ding M, Lau J, Li M, Wang C, Xu X, Hao G, Papandrea B, Shakir I, Dunn B, Huang Y, Duan X. *Science*, 2017, 356: 599–604
2 Li B, Dai F, Xiao Q, Yang L, Shen J, Zhang C, Cai M. *Energy Environ Sci*, 2016, 9: 102–106
3 Wang RT, Lang JW, Yan XB. *Sci China Chem*, 2014, 57: 1570–1578
4 Faraji S, Ani FN. *Renew Sustain Energy Rev*, 2015, 42: 823–834
5 Wang X, Kong D, Wang B, Song Y, Zhi L. *Sci China Chem*, 2016, 59: 713–718
6 Kim HK, Bak SM, Lee SW, Kim MS, Park B, Lee SC, Choi YJ, Jun SC, Han JT, Nam KW, Chung KY, Wang J, Zhou J, Yang XQ, Roh KC, Kim KB. *Energy Environ Sci*, 2016, 9: 1270–1281
7 Boukhalfa S, Evanoff K, Yushin G. *Energy Environ Sci*, 2012, 5: 6872–6879
8 Huang Y, Zhong M, Huang Y, Zhu M, Pei Z, Wang Z, Xue Q, Xie X, Zhi C. *Nat Commun*, 2015, 6: 10310
9 Sun J, Li W, Zhang B, Li G, Jiang L, Chen Z, Zou R, Hu J. *Nano Energy*, 2014, 4: 56–64
10 Hao P, Cui G, Shi X, Xie J, Xia X, Sang Y, Wong CP, Liu H, Tang B. *Chin J Chem*, 2017, 35: 699–706
11 Yu Z, Tetard L, Zhai L, Thomas J. *Energy Environ Sci*, 2015, 8: 702–730
12 Zhang Z, Ma W, Xu B, Zhou X, Wang C, Xie Z, Liu L, Ma Y. *Sci China Chem*, 2018, 61: 192–199
13 Acerce M, Voiry D, Chhowalla M. *Nat Nanotech*, 2015, 10: 313–318
14 Dubal DP, Ayyad O, Ruiz V, Gómez-Romero P. *Chem Soc Rev*, 2015, 44: 1777–1790
15 Li X, Xiao X, Li Q, Wei J, Xue H, Pang H. *Inorg Chem Front*, 2018, 5: 11–28
16 Zhang WJ, Huang KJ. *Inorg Chem Front*, 2017, 4: 1602–1620
17 Zhang F, Liu T, Li M, Yu M, Luo Y, Tong Y, Li Y. *Nano Lett*, 2017, 17: 3097–3104
18 Nyström G, Marais A, Karabulut E, Wågberg L, Cui Y, Hamedi MM. *Nat Commun*, 2015, 6: 7259
19 Yu D, Goh K, Wang H, Wei L, Jiang W, Zhang Q, Dai L, Chen Y. *Nat Nanotech*, 2014, 9: 555–562
20 Wang Q, Yan J, Wang Y, Wei T, Zhang M, Jing X, Fan Z. *Carbon*, 2014, 67: 119–127
21 Hao P, Zhao Z, Leng Y, Tian J, Sang Y, Boughton RI, Wong CP, Liu H, Yang B. *Nano Energy*, 2015, 15: 9–23
22 Hao P, Tian J, Sang Y, Tuan CC, Cui G, Shi X, Wong CP, Tang B, Liu H. *Nanoscale*, 2016, 8: 16292–16301
23 Gomez J, Kalu EE. *J Power Sources*, 2013, 230: 218–224
24 Ma W, Chen S, Yang S, Chen W, Weng W, Cheng Y, Zhu M. *Carbon*, 2017, 113: 151–158
25 Faraji S, Ani FN. *J Power Sources*, 2014, 263: 338–360
26 Chen LY, Hou Y, Kang JL, Hirata A, Chen MW. *J Mater Chem A*, 2014, 2: 8448–8455
27 Du W, Xu X, Zhang D, Lu Q, Gao F. *Sci China Chem*, 2015, 58: 627–633
28 Ge F, Li MM, Ye H, Zhao BX. *J Hazard Mater*, 2012, 211-212: 366–372
29 Rapti S, Pournara A, Sarma D, Papadas IT, Armatas GS, Hassan YS, Alkordi MH, Kanatzidis MG, Manos MJ. *Inorg Chem Front*, 2016, 3: 635–644
30 Badruddoza AZM, Shawon ZBZ, Tay WJD, Hidajat K, Uddin MS. *Carbohydrate Polym*, 2013, 91: 322–332
31 Demirbas A. *J Hazard Mater*, 2008, 157: 220–229
32 Yu D, Wang H, Yang J, Niu Z, Lu H, Yang Y, Cheng L, Guo L. *ACS Appl Mater Interfaces*, 2017, 9: 21298–21306
33 Fu F, Dionysiou DD, Liu H. *J Hazard Mater*, 2014, 267: 194–205
34 Homhuan NB, Imwiset KJ, Bureekaew S, Ogawa M. *Clay Sci*, 2017, 21: 21–28
35 Tahmasebi E, Yamini Y. *Microchim Acta*, 2014, 181: 543–551
36 Zhou Y, Zhou W, Hou D, Li G, Wan J, Feng C, Tang Z, Chen S. *Small*, 2016, 12: 2768–2774
37 Chen Y, Zhang W, Yang S, Hobiny A, Alsaedi A, Wang X. *Sci China Chem*, 2016, 59: 412–419
38 Li Y, Zhang J, Xu C, Zhou Y. *Sci China Chem*, 2016, 59: 95–105
39 Fan L, Zhang N, Sun K. *RSC Adv*, 2014, 4: 21419
40 Hu J, Tao P, Wang S, Liu Y, Tang Y, Zhong H, Lu Z. *J Mater Chem A*, 2013, 1: 6558
41 Tao P, Hu J, Wang W, Wang S, Li M, Zhong H, Tang Y, Lu Z. *RSC Adv*, 2014, 4: 13518
42 Cho HH, Wepasnick K, Smith BA, Bangash FK, Fairbrother DH, Ball WP. *Langmuir*, 2010, 26: 967–981
43 Lee J, Lee DM, Kim YK, Jeong HS, Kim SM. *Small*, 2017, 13: 1701131
44 Kolhe P, Kannan RM. *Biomacromolecules*, 2003, 4: 173–180
45 Gu X, Yang Y, Hu Y, Hu M, Wang C. *ACS Sustain Chem Eng*, 2015, 3: 1056–1065
46 Wei B, Liang H, Zhang D, Wu Z, Qi Z, Wang Z. *J Mater Chem A*, 2017, 5: 2844–2851
47 Pandey K, Yadav P, Mukhopadhyay I. *Phys Chem Chem Phys*, 2015, 17: 878–887
48 Li Q, Li K, Sun C, Li Y. *J Electroanal Chem*, 2007, 611: 43–50
49 Wang Y, Zhang Y, Pei L, Ying D, Xu X, Zhao L, Jia J, Cao X. *Sci Rep*, 2017, 7: 41523